Structure-dependence of the atomic-scale mechanisms of Pt electrooxidation and dissolution

Timo Fuchs[1], Jakub Drnec[2], Federico Calle-Vallejo[3], Natalie Stubb[4], Daniel J. S. Sandbeck[5,6], Martin Ruge[1], Serhiy Cherevko[5], David A. Harrington[4] & Olaf M. Magnussen[1*]

[1]*Institut für Experimentelle und Angewandte Physik, Christian-Albrechts-Universität zu Kiel, Olshausenstr. 40, 24098 Kiel, Germany*

[2]*Experimental division, European Synchrotron Radiation Facility, 71 Avenue des Martyrs, 38000 Grenoble, France*

[3]*Departament de Ciència de Materials i Química Fisica & Institut de Química Teòrica i Computacional (IQTCUB), Universitat de Barcelona, Martí i Franquès 1, 08028 Barcelona, Spain.*

[4]*Chemistry Department, University of Victoria, Victoria, British Columbia, V8W 2Y2, Canada*

[5]*Helmholtz-Institute Erlangen-Nürnberg for Renewable Energy (IEK-11), Forschungszentrum Jülich GmbH, 91058 Erlangen, Germany*

[6]*Department of Chemical and Biological Engineering, Friedrich-Alexander-Universität Erlangen-Nürnberg, 91058 Erlangen, Germany*

* Corresponding author

Abstract

Platinum dissolution and restructuring due to surface oxidation are primary degradation mechanisms that limit the lifetime of Pt-based electrocatalysts for electrochemical energy conversion. Here, we studied well-defined Pt(100) and Pt(111) electrode surfaces by in situ high-energy surface X-ray diffraction, on-line inductively coupled plasma mass spectrometry, and density functional theory calculations, to elucidate the atomic-scale mechanisms of these processes. The locations of the extracted Pt atoms after Pt(100) oxidation reveal distinct differences from the Pt(111) case, which explains the different surface stability. The evolution of a specific stripe oxide structure on Pt(100) produces unstable surface atoms which are prone to dissolution and restructuring, leading to one order of magnitude higher dissolution rates.

Introduction

The degradation of Pt catalysts for the cathode reaction in fuel cells is linked to their electrooxidation and dissolution.[1] Both these processes are arguably even more complex than the actual energy conversion via oxygen reduction and have been studied for a long time, mainly on polycrystalline and supported nanoparticle catalysts. Single-crystal studies offer the prospect of a more detailed understanding of these processes at the atomic level [2–11]. Some such studies followed these processes with potential cycling, where it is known that the surface restructuring over many cycles leads to a roughened surface, and that dissolution is enhanced during oxide reduction.[12–22] Explanation of this behaviour generally invokes a place exchange (PE) process, in which a Pt surface

atom leaves its lattice site and oxygen penetrates into the metal lattice. On Pt(111), pioneering studies demonstrated that PE can be directly observed by surface X-ray diffraction (SXRD).[4,5] More recent SXRD measurements confirmed this [18,23–25] and allowed structural refinement, showing that the exchanged Pt atom lies 2.4 Å above its original lattice site,[18] in good agreement with density functional theory (DFT) studies of this process.[26–28] In contrast to Pt(111), other Pt crystal faces show distinct differences in the oxidation and dissolution behaviour.[10,12,14,29] This has been qualitatively explained by the more open arrangement of the surface atoms, but precise atomic level data are scarce. Thus, clear structure-reactivity relationships, which e.g. would guide the development of tailored Pt catalysts, are still lacking.

We here present detailed structural studies, focussing on the precise atomic motions in these early stages of oxidation. By correlating in situ SXRD measurements, which reveal how the place-exchanged Pt atoms are arranged in the initial stages of surface oxidation, with detailed DFT studies of this process, a direct comparison of the elementary processes underlying Pt(111) and Pt(100) oxidation becomes possible. Our study reveals a sharply different mechanism for the oxidative extraction of Pt atoms out of the two surfaces, providing a detailed explanation for the enhanced dissolution on Pt(100), observed by on-line mass spectroscopy.

Results

Dissolution and surface restructuring by electrooxidation. According to cyclic voltammetry (CV) studies, the onset of Pt oxidation is marked on these two surfaces by a current peak above

1.0 V (labelled O_{ads} in Fig. 1b, c and Extended Data Fig. 1). However, the CV of Pt(100) irreversibly changes in subsequent cycles, whereas that of Pt(111) remains stable for an upper potential limit (UPL) of $\lessapprox$ 1.15 V and thus can be mistaken for an oxidation process without surface restructuring.[7,12,29] The (ir)reversibility of the CVs is mirrored in the Pt dissolution rates obtained by inductively coupled plasma mass spectrometry (ICP-MS) in a (capillary) scanning flow cell (CSFC and SFC) with results summarised in Fig. 1a,d. The facet dependent trends are readily apparent. At sweep rates of $\gtrapprox$ 10 mV/s, no dissolution is seen for either surface for CVs with an UPL of 1.0 V, in agreement with previous results.[14,16] When increasing the UPL, the onset of significant anodic dissolution due to Pt oxidation is observed for Pt(100) as soon as the O_{ads} peak begins, while for Pt(111) the onset only occurs at potentials above 1.2 V. Cathodic dissolution during the oxide reduction is observed for both surfaces at UPLs $\geq$ 1.1 V; however, the dissolution of Pt(100) exceeds that of Pt(111) by about one order of magnitude. The onset and amount of dissolution depends on the precise time-potential program, reflecting the slow oxidation kinetics,[14] but the enhanced rates for Pt(100) as compared to Pt(111) are found in all experiments. It is noted that the amount of oxide formed in both cases is comparable, only about 20% higher for Pt(100) (as seen from the integral of the oxidation peaks in the CVs). Thus, the significant difference in dissolution rates points towards a fundamentally different oxidation behaviour of the two surfaces. Similar facet dependent trends have been found in previous comparative studies of the dissolution behaviour of Pt(100) and Pt(111)[14,16], but these do not link the difference to the oxide structure and also do not provide mechanistic explanations, due to the lack of knowledge on the structural changes during surface oxidation.

Rev. Cmt. 1)

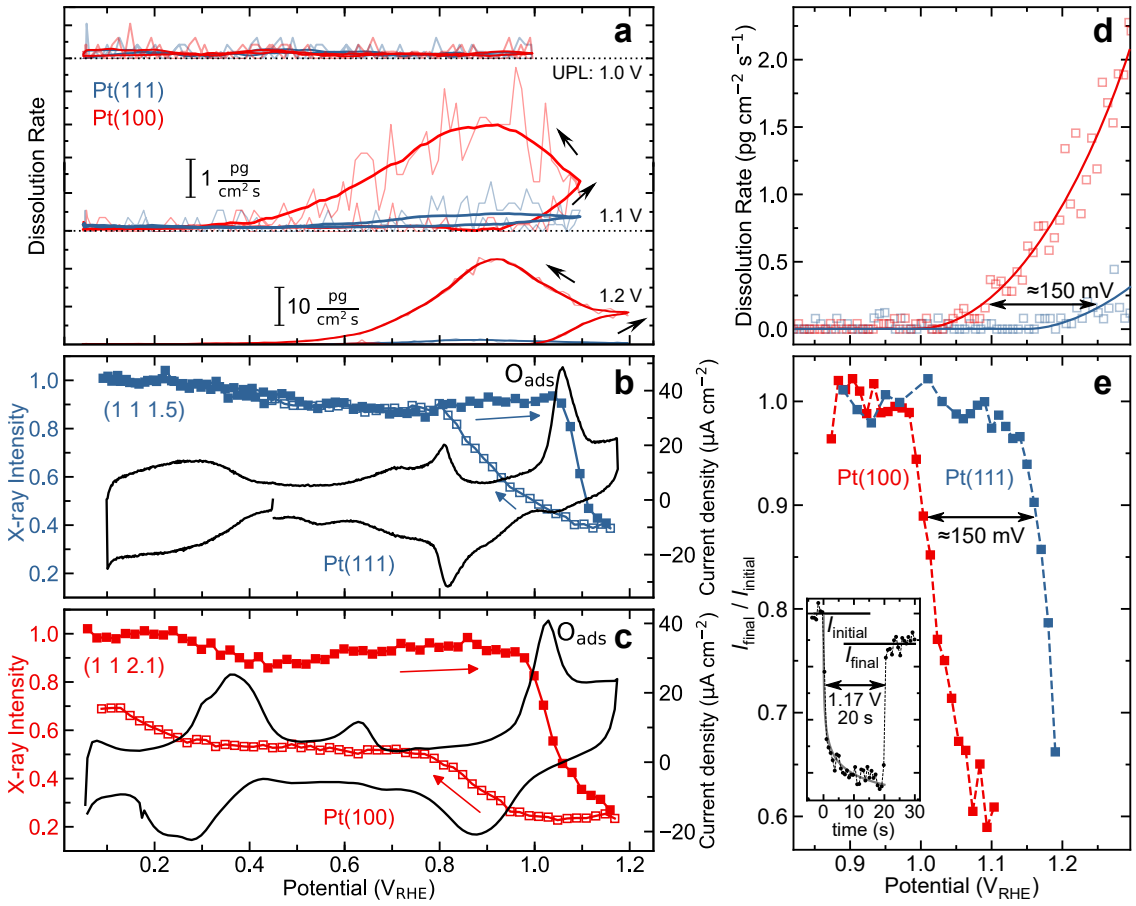

Fig. 1. Dissolution and atomic-scale structural changes during Pt oxidation. **(a)** Pt dissolution during cycles at 50 mV/s to increasingly positive potential limits (UPL) obtained using the capillary scanning flow cell, illustrating that the cathodic dissolution during oxide reduction is significantly more pronounced on Pt(100). X-ray intensity changes at the anti-Bragg positions of selected crystal truncation rods and simultaneously measured cyclic voltammograms of **(b)** Pt(111) (data taken from Ref. 23) and **(c)** Pt(100) during potential cycles at 20 mV/s. Pt place exchange (PE), indicated by the intensity drop at the O_{ads} peak, is initially fully reversible on Pt(111), whereas for Pt(100) it always results in irreversible surface restructuring. **(d)** Potential-dependent Pt dissolution rates during a positive sweep at 10 mV/s obtained with the scanning flow cell, showing the onset of anodic dissolution. **(e)** Reversibility of the PE process, determined by potential step experiments, where the potential was changed for 20 s from 0.47 V in the double layer range to a potential in the oxidation regime and then moved back to 0.47 V (illustrated in inset). The relative changes in X-ray intensity indicate that irreversible Pt surface restructuring starts at $\approx$ 150 mV higher potentials on Pt(111) than on Pt(100).

The atomic scale origin of this difference was investigated by *in situ* surface X-ray diffraction (SXRD). This technique determines the exact positions of surface atoms during the initial stages of oxidation, which can then be linked to the dissolution and surface restructuring mechanisms. For a qualitative assessment of the influence of surface orientation, we first followed reflections near the anti-Bragg positions of the crystal truncation rods (CTRs). Those are sensitive to the distortion of the ideal Pt lattice and the extraction of Pt atoms out of the surface in the place exchange process.[4,5,23] Performing such measurements during potential cycles revealed that on both surfaces the onset of PE coincides with the O_{ads} peak maximum (0.98 V and 1.04 V on Pt(100) and Pt(111) respectively), but that the subsequent structural response is very different (Fig. 1b,c).

PE on Pt(100) results in irreversible surface structural changes, as indicated by the irreversible decrease in X-ray intensity after completion of one potential cycle. In contrast, the PE process on Pt(111) is initially fully reversible [4,23] and only results in irreversible surface restructuring, if the upper potential limit exceeds 1.15 V. Here, the onset of irreversibility occurs above a critical coverage of extracted Pt atoms [23], which depends on potential and time in the oxidation regime. A more quantitative comparison of the onset of irreversible intensity changes, obtained in potential step experiments (Fig. 1e), indicates that these occur on Pt(111) at about 150 mV more positive potentials than on Pt(100), closely mirroring the onset of Pt dissolution (Fig. 1d). This unambiguously demonstrates that on single crystal surfaces dissolution and irreversible surface structural changes are linked. Although the latter was already stated in the work of Lopes et al.,[14,15] here the dissolution behavior was attributed to irreversible Pt oxide formation at the peak around 1 V, where on Pt(111) oxidation is still largely reversible. Furthermore, our observations resemble the *in situ*

Raman spectroscopy data by Huang et al.,[10] who reported that bands associated with the formation of 3D α-PtO_2 oxide phase occur at 200 mV more negative potentials on Pt(100) than on Pt(111). However, PE on Pt(111) was here proposed to occur only at $\geq$ 1.3 V, which is at variance with the SXRD results. Therefore, a clear correlation between the precise oxide structure of different Pt surfaces, its reversibility, and its effect on the dissolution is still lacking.

Atomic-scale structure of the Pt oxide. To assess the difference between the reversible and irreversible structural processes, we performed a detailed potential-dependent surface crystallographic analysis of an extended set of CTRs. An overview of all measured data sets is given in Supplementary Note 1. For Pt(111) the surface atom arrangement was determined in our previous study.[18,23] At low coverage the PE was found to result only in an $\approx$ 2 Å vertical displacement of the extracted Pt atom (Pt_{ex}), whereas the in-plane position remains the same. The Pt_{ex} thus is located directly above its original site, which is now vacated or filled with oxygen. Previous density functional theory (DFT) studies also found this unusual geometry and indicated that it is stabilised by three neighbouring oxygen adsorbates on the Pt(111) surface.[27]

Similar structural characterisation of the initial stages of Pt(100) oxidation is more difficult, because unlike on Pt(111), the surface oxide continuously evolves over timescales of hours. This strongly impedes conventional SXRD measurements, which typically require 1 - 2 h recording time. We therefore performed *in situ* measurements by the novel technique of high-energy surface X-ray diffraction (HESXRD)[30], which allows collection of many CTRs in just a few minutes, i.e., in a time period over which the structural changes in the oxide are negligible. Examples

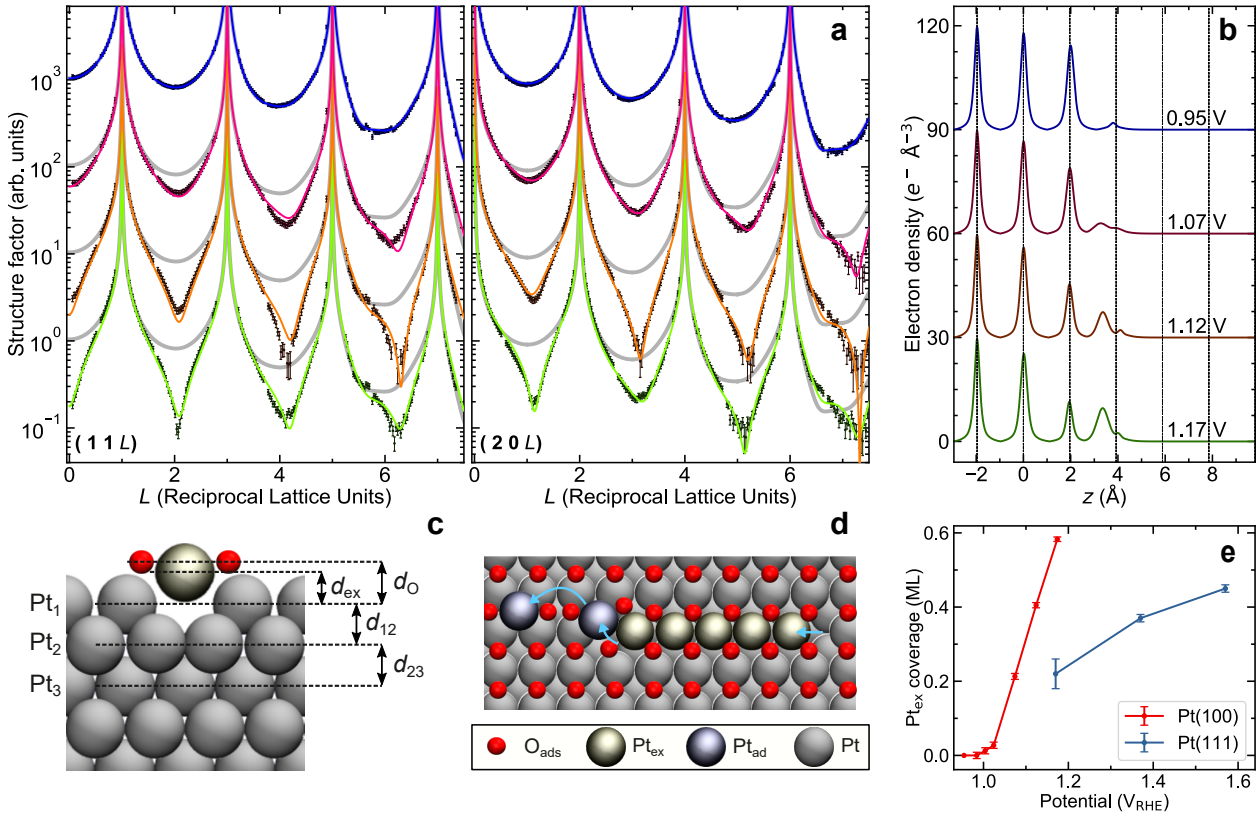

Fig. 2. Atomic structure of the place exchange site on Pt(100). **(a)** Two of the 11 measured crystal truncation rods (CTR) of Pt(100), obtained by *in situ* high energy surface x-ray diffraction measurements (68 keV) at a potential slightly negative (0.95 V) and three potentials positive (1.07, 1.12 and 1.17 V) of the O_{ads} peak in the cyclic voltammogram (Fig. 1b, Extended Data Fig. 1). The latter exhibit significantly decreased intensities and correspond to surfaces in which 20 to 60 % of the Pt atoms underwent place exchange. Each set of CTRs was recorded within 550 s, starting 300 s after the potential was established. The full CTR sets are given in Extended Data Fig. 3. In addition to the experimental data, which are offset by a factor of 10 with respect to each other, the best fit (coloured lines) and the CTR fits for the smooth surface at 0.95 V (grey line) are shown. **(b)** Electron density profile along the surface normal, obtained from the quantitative modelling of the CTRs. The bulk Pt lattice positions are indicated by dashed vertical lines. **(c)** Side and **(d)** top view of the atomic arrangement of the extracted Pt atoms (the labels correspond to the parameters in Supplementary Table 2). **(e)** Potential-dependent Pt_{ex} coverage on Pt(100), obtained from the crystal truncation rod analysis, compared with the Pt_{ex} coverage on Pt(111) (taken from Ref. 18).

of the CTRs measured on Pt(100) are shown in Fig. 2a (see Extended Data Fig. 3 for the full data set). Measurements at 0.12 V (Extended Data Fig. 2 and Supplementary Figure 2, see also Supplementary Note 2 for further details on the data analysis) confirm that the initial surface is unreconstructed and exhibits negligible roughness. At potentials slightly negative of the O_{ads} peak in the CV, adsorption of oxygen species is signalled by changes in the Pt surface relaxation and increased statistical deviations of Pt surface atoms from ideal lattice positions, characterised by larger Debye-Waller factors. After the onset of PE, the intensity of all CTRs substantially decreases. This change cannot be described by Pt_{ex} in an on-top geometry, as in the case of Pt(111), or in conventional hollow or bridge sites atop the Pt surface. (see Supplementary Note 3 for details on the data analysis). A good description of the large HESXRD data sets was only possible by models that assume that the majority of extracted Pt atoms reside in bridge sites with vertical positions that are merely 1.40 Å (d_{ex} in Fig. 2c) above the Pt(100) surface plane (Fig. 2b). These models allowed fitting all of the CTR data obtained at different oxidation potentials, with very similar structure parameters, apart from the Pt_{ex} coverage, which continuously increased up to 0.6 ML with increasing potential (Fig. 2e, see Supplementary Table 2 for all structural parameters). It is noted that on Pt(111) the Pt_{ex} coverage increases more moderately, to 0.45 ML at 1.57 V.[18]

The low vertical position of the Pt_{ex} is sterically incompatible with species residing atop the surface, but can be readily explained by Pt atoms that are bound via surface or subsurface oxygen to the centre of a vacancy dimer. The resulting geometry distinctly differs from that of Pt_{ex} on Pt(111), both in terms of the coordination as well as the distances of the Pt_{ex} to the neighbouring atoms in the Pt surface layer (about 0.2 Å larger) and the vertical spacing of the Pt_{ex} atoms from

the layer below (d_{ex} >2.23 Å[18] on Pt(111), d_{ex} <1.42 Å on Pt(100), see Supplementary Table 2). Formation of such a vacancy dimer requires extraction of a second Pt atom from the surface layer (Pt_{ad}), which can be positioned as an adatom on the neighbouring Pt surface or as a slightly more protruded atom on the end of the dimer. However, Pt_{ex} and Pt_{ad} are not necessarily generated in equal numbers. For example, only one additional Pt_{ad} would be produced in the growth of a Pt oxide chain structure (Fig. 2d), similar to those found in scanning tunneling microscopy studies[31,32] and density functional theory (DFT) calculations [26] of Pt(111) oxidation in the gas-phase. In this case, the Pt_{ad} would only be formed as a minority species, not necessarily detectable in SXRD experiments. Indirect support for this scenario comes from CTR data obtained at 0.12 V after oxide reduction, which is shown in Extended Data Fig. 2. Here, Pt_{ad} in hollow sites are clearly present, but at coverages that are ten times lower than that of the Pt_{ex} in the corresponding oxide film. This suggests that also on Pt(100) the majority of Pt_{ex} directly return into surface vacancies after reduction.

Mechanism of oxide formation and Pt dissolution. To further confirm the proposed structural development, we performed a comparative DFT study of the PE and Pt dissolution processes. We first calculated the Pourbaix diagrams for Pt(111) and Pt(100) (Extended Data Fig. 5) to determine the most stable oxygen coverage and adsorption sites as a function of pH and applied potential. The stabilization granted by water wetting was taken into account in the free energy assessment of all species (see the Methods section for further details).

In good agreement with the experimental data (Fig. 1b,c), platinum extraction is calculated to be

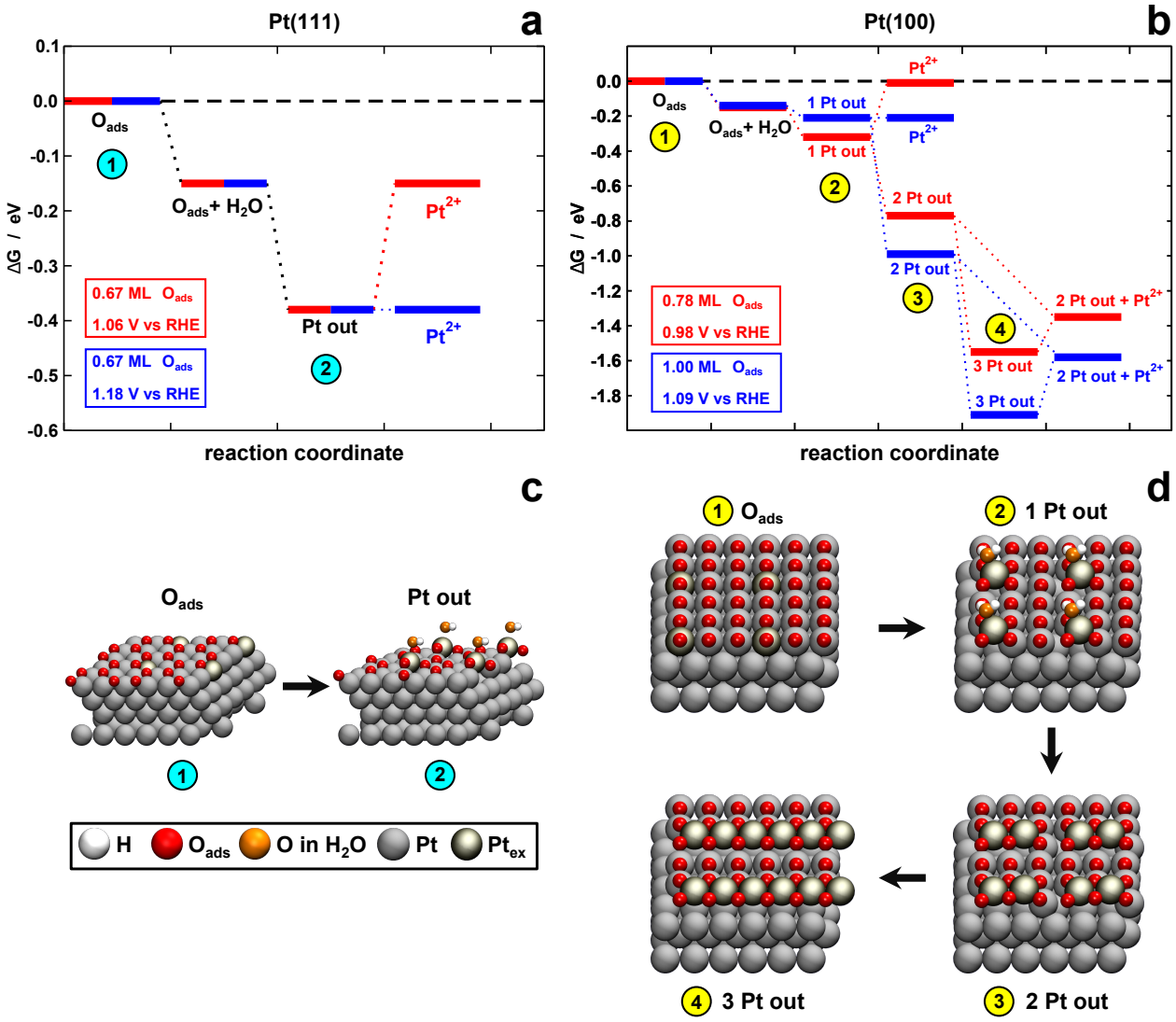

Fig. 3. Atomistic view of place exchange and dissolution on Pt(111) and Pt(100). Free energy landscapes of place exchange and dissolution obtained by density functional theory calculations of **(a)** Pt(111) and **(b)** Pt(100). Corresponding schematics of the main steps in the reaction pathway are shown in **(c)** and **(d)** for Pt(111) and Pt(100), respectively. In both cases, surface wetting by H_2O is accounted for and observed to aid the extraction process (for clarity, H_2O is not shown in step (3) and (4) of **(d)**). Dissolution of the first Pt_{ex} in form of Pt^{2+} is not favoured at low potentials (1.06 V on Pt(111), 0.98 V on Pt(100)), but becomes energetically favourable at higher potentials (1.18 V on Pt(111), 1.09 V on Pt(100)). Further Pt extraction proceeds differently on Pt(100), where a second and third extraction is favourable, leading to an extended extracted stripe of Pt atoms. Parallel to the stripe extraction process, dissolution can already occur at 0.98 V through detachment of one of Pt atoms in the dimer formed after the second stripe extraction. Top and side views of the surfaces are provided in Extended Data Fig. 6.

thermodynamically favourable starting from 1.06 V at $\theta_{\mathrm{O}} \approx 0.67$ ML on Pt(111) and ≥ 0.98 V at $\theta_{\mathrm{O}} \approx 0.78$ ML for Pt(100) (Extended Data Fig. 4). According to energy calculations of the various steps in the PE process (Fig. 3a,b), PE starts on Pt(111) with O_{ads} adsorption (Fig. 3, step 1) followed by the extraction of a Pt atom (step 2). In line with previous SXRD [18,23] and DFT [27] studies, the extracted Pt atom is located above a vacancy, and is coordinated to three O_{ads} atoms (Fig. 3c, Extended Data Fig. 6). Our extraction pathway on Pt(111) is similar to the one reported by Eslamibidgoli and Eikerling,[27] who found that PE starts at oxygen coverages between 0.59 and 0.75 ML. The pathway for PE on Pt(100) is substantially different from that on Pt(111) (Fig. 3b). Although it also starts by O_{ads} adsorption and the extraction of a Pt atom, the high O_{ads} coverage allows Pt extraction to immediately proceed at neighbouring sites. Hence, there is a consecutive extraction of Pt atoms that ultimately leads to the creation of a stripe of protruded atoms. In agreement with our experiments, the Pt_{ex} are not located above their original lattice sites but move sideways to a square-planar site where they are coordinated to four O_{ads} atoms. Because of the latter, this arrangement is strongly stabilised, contrary to Pt(111), where stripe-like structures only lead to small gains in free energy as compared to isolated Pt_{ex}.[26] The larger O_{ads} coordination around the Pt_{ex} may lead to the Raman signature resembling $\mathrm{PtO_2}$, as observed for Pt(100) in this potential range.[10] Furthermore, we note that the first Pt_{ex} of each stripe has to deviate from the perfect square-planar site for steric reasons (see Pt_{ex} positions after first and second extraction), resulting in the more weakly bound Pt_{ad} species postulated above.

The differences in Pt(111) and Pt(100) anodic dissolution upon oxidation, i.e., the conversion of Pt_{ex} to a Pt ion (assumed to be Pt^{2+})[33], can be ascribed to the different Pt extraction process. On

Pt(111), the Pt_{ex} are initially arranged directly above the vacancy and this is thermodynamically more stable than a Pt^{2+}-vacancy pair (Fig. 3a and Methods section). Only after the potential increases to 1.18 V does the dissolution become energetically favourable (Fig. 3a and Extended Data Fig. 4). The situation is different on Pt(100) (Fig. 3b), where the dissolution is not favoured at 0.98 V during the first extraction, but the atomic arrangement formed after the second extraction is prone to dissolution. DFT calculations show this process to be exothermic and to result in the same structure after removal of a Pt_{ex} atom from the second and third extraction state. The reason for this is that in the case of dissolution from the second extraction state subsequent extraction of a further Pt surface atom occurs. This leads to stabilization of the system, because the formed dimer is now better positioned in the triple vacancy. Thus, the Pt_{ex} atoms formed in the initial stages of stripe formation as well as the more weakly bound Pt_{ad} at the ends of stripes are prone to dissolution. This explains the higher anodic dissolution rates and lower dissolution potentials of Pt(100) as compared to Pt(111), where no similar destabilised atoms exist. After the potential exceeds that for 1 ML O_{ads} coverage (1.09 V), the dissolution can also take place during the first extraction step.

The initial reversibility of PE and stability against cathodic dissolution on Pt(111) can be attributed to the on-top arrangement found in our SXRD and DFT studies, when the Pt_{ex} coverage is low and the Pt(111) lattice around the vacancy on which the O_{ads} atoms are adsorbed remains intact. This on-top geometry facilitates back insertion of the Pt_{ex} into the vacancy after desorption of oxygen in the reduction process (ΔG_{ex} = -0.5 eV at θ_O = 0.44 ML, Extended Data Fig. 4) rather than formation of a Pt adatom - vacancy pair via detachment or dissolution in the form of Pt^{2+}

as discussed in Ref. 15. At higher Pt_{ex} coverage the oxide surface structure is more complex, impeding straightforward conclusions on the exact restructuring process. However, the increasing deviations of the Pt_{ex} from the on-top positions, observed by SXRD,[18] suggest a gradual loss of the overall integrity of the Pt surface lattice, which may account for the irreversible surface roughening during subsequent oxide reduction as well as for Pt cathodic dissolution. In contrast, on Pt(100) we expect Pt adatoms and Pt^{2+} formation directly from the ends of the Pt_{ex} stripes during oxide reduction. Similarly, adatoms and Pt^{2+} are also expected to form during the oxide reduction, i.e., upon a decrease in the O_{ads} coverage. While the stripes are shortened, the remaining destabilised Pt_{ad} at the end of the stripe are more likely to dissolve or form adatoms.

Conclusion

In conclusion, the onset potentials of anodic dissolution on Pt(100) and Pt(111) correspond to the onset of irreversibility in the extraction of the first Pt atoms from their lattice sites as the surface is oxidized. According to our combined SXRD and DFT studies, the marked difference in behaviour of the two surfaces has its origin in the different atomic structures of the initial oxide. On Pt(111), the extracted Pt atom lies directly above its original site, and reversibility for low coverages is explained by its facile return to that site. However, on Pt(100) the extracted Pt atom moves laterally away from its original site and initiates immediate extraction of a second atom, leading to the formation of a stripe structure. This mechanism produces unstable surface atoms at the stripe ends, which can be dissolved both during the oxidation itself and during subsequent oxide reduction, making the process irreversible from its onset.

As shown by our data, the precise Pt extraction mechanisms during oxidation and the accompanying dissolution differ substantially on different Pt facets. This sensitivity of Pt electrocatalyst degradation on surface structure has to be taken into account in the quest for a knowledge-based approach, where highly stable catalysts are ideally predicted *ab initio*. While our study represents the first step in developing an atomistic picture of these processes for surfaces other than Pt(111) (which may be considered as an atypical case according to the results presented here), further studies are necessary, especially of more open high-index surfaces. Such detailed insight into the degradation mechanisms of structurally defined model systems is an important prerequisite for the challenging task of *ab initio* modelling the stability of real catalyst particles and, ultimately, developing rational strategies for the design of catalysts with improved stability.

Methods

Sample preparation. All experiments employed cylindrical Pt single crystals (Mateck, Crystal Preparation Laboratory) and Ar-purged $0.1\,\mathrm{M}$ $HClO_4$ solution made from ultrapure water and suprapur® perchloric acid (Merck). Potentials were measured versus Ag/AgCl ($KCl_{sat.}$, SFC-ICP-MS or 3.4 M KCl, SXRD) reference electrodes but are reported against the reversible hydrogen electrode (RHE). The Pt crystals were initially cleaned in an ultra-high vacuum chamber using repeated Ar^+-ion bombardment and subsequent annealing at 900 °C in 10^{-6} mbar oxygen. Prior to each experiment, the Pt crystals were prepared by flame annealing with a butane torch (SFC-ICP-MS) or by annealing under 2 % CO/ 98 % Ar in an induction oven (SXRD). Subsequently, the sample was cooled in a flow of Ar/H_2 (SFC-ICP-MS) or 2 % CO/ 98 % Ar (SXRD) and transferred

to the cell protected either by a drop of Ar saturated ultrapure water or the adsorbed CO layer (SXRD, only Pt(100)). Immersion into the electrolyte was performed under potential control at potentials in the double layer regime. After immersion, remaining adsorbed CO was removed by anodic stripping.

Dissolution measurements. The dissolution measurements at low scan rate of 10 $\mathrm{mV{\cdot}s^{-1}}$ to resolve the onset potentials of dissolution were conducted using the classical scanning flow cell coupled to an inductively coupled plasma mass spectrometer technique (referred to as SFC-ICP-MS, NexION 300X, Perkin Elmer). The working electrode (WE) had a contact area of $0.035\,\mathrm{cm}^2$. The flow rate of the SFC-ICP-MS was ca. $170\,\mu\mathrm{L}\cdot\mathrm{min}^{-1}$. ^{187}Re was used as an ICP-MS internal standard for platinum. A graphite rod was used as a counter electrode and a double junction Ag/AgCl (Metrohm) as a reference electrode. Details on the SFC-ICP-MS measurements are given in Ref. 34, 35. The CV experiments at relatively fast scan rates were carried out using a modification to the SFC-ICP-MS, referred to here as the CSFC-ICP-MS (capillary SFC-ICP-MS), which allows for significantly increased time-potential resolution.[36] By inserting a small capillary directly above the working electrode (Supplementary Figure 9) and connecting directly to the ICP-MS via self-aspiration (bypassing the use of the peristaltic pump) delay times between the dissolution on the WE and ICP-MS detection can be reduced from ca. 25 to 3 s. Reduced delay times and shorter tubing distances limit the dispersion of dissolved species, and therefore enhance the resolution of dissolution rate profiles, e.g. to clearly separate anodic and cathodic dissolution signals.[37] The relatively fast flow rate of $580\,\mu\mathrm{L}\cdot\mathrm{min}^{-1}$ resulted in a collection efficiency >99 %. Further details on this new technique can be found in Ref. 38.

Electrochemical cell for surface x-ray diffraction. All Surface X-ray Diffraction (SXRD) experiments employed the established SXRD electrochemical cell, described in Ref. 39. Inside this cell, the upward facing single-crystalline surface of the crystal sample is in contact with the electrolyte via a free-standing meniscus. This geometry is similar to the hanging meniscus geometry commonly used in single crystal electrochemistry and minimises contributions from the defect-rich edges of the crystal. The amount of electrolyte inside the cell was controlled remotely using a motorised pump system with a precision of 1 µl. To prevent oxygen contamination, the meniscus was kept in Ar atmosphere and the electrolyte reservoirs were continuously purged with Ar. We used a high-purity Pt foil with a surface area of about $120\,\mathrm{mm}^2$ as counter electrode and a Ag/AgCl (3.4 M KCl, eDaq) reference electrode. The reference electrode was connected by a micron-sized hole to a glass capillary, which was filled with 0.1 M $HClO_4$ and served as Luggin capillary and salt bridge. This arrangement effectively ensured negligible leakage of KCl from the reference electrode to the cell. The cell and all glassware and tubing that were in contact with the electrolyte had been previously cleaned by soaking in a 4:1 mixture of concentrated H_2SO_4 and 30 % H_2O_2 for at least 1 day. Afterwards, all materials were rinsed and boiled repeatedly in high-purity water (Elga purelab ultra 18.2 MΩ cm). Cyclic voltammograms (CVs) of Pt(111) and Pt(100) in 0.1 M $HClO_4$ in the double layer potential region, prepared in this way and measured in the SXRD electrochemical cell, are shown in Extended Data Figure 1. For both surfaces, the voltammograms are in good agreement with those reported in the literature.[29] CVs up to $0.6\,\mathrm{V}$ were recorded at the beginning of every SXRD experiment to check that a high surface quality had been obtained by the annealing process.

Surface x-ray diffraction setup. All SXRD experiments were performed at undulator beamlines ID03 and ID31 of the European Synchrotron Radiation Facility using a six-circle geometry and constant incident angle. A schematic illustration of the experimental setup is shown in Supplementary Figure 6. The crystal inside the SXRD cell was positioned with the surface facing upwards. Conventional SXRD studies were performed at beamline ID03 and focused on kinetic studies of the Pt oxidation process by measuring the X-ray intensity at a fixed position along a crystal truncation rod (CTR). Similar as in our previous studies,[17,18,23,24,40] these measurements employed a photon energy of 22.5 keV, a (vert./hor.) beam size of 45×750 $\mu\mathrm{m}^2$ and an angle of incidence of 0.3°. A small 2D detector (Maxipix) mounted on the diffractometer arm was used to simultaneously measure the crystal truncation rod (CTR) intensity and the background intensity with a time resolution of 0.1 s. The structure factor of the CTR at the studied reciprocal space position was determined by first subtracting the background intensity and then taking the square root of the integrated diffraction rod intensity.

Operando high-energy SXRD (HESXRD) measurements of the Pt(100) CTRs were performed at the high-energy beamline ID31 at a photon energy of 68 keV. To enhance the surface contribution, the incident angle was kept at 0.05°, which is below the critical angle of total external reflection. The beam size at the sample position was 12×48 $\mu\mathrm{m}^2$. The orientation of the surface normal direction was aligned better than 0.005° relative to the in-plane rotation axis, to ensure that the angle of incidence did not change during sample rotation. The diffracted X-ray intensity was recorded with a stationary, large-area X-ray detector (Pilatus 2M CdTe), which was positioned 73 cm behind the sample. This allowed covering a range of up to $12\,\mathrm{\AA}^{-1}$ momentum transfer perpendicular

to the surface and a range of about $\pm 5.5\,\text{Å}^{-1}$ momentum transfer parallel to the surface. The tilt angles between the detector plane and the incident beam direction were determined by recording the Debye-Scherrer rings of a CeO_2 powder calibration standard and analyzing these data with the *pyFAI* software.[41] The calculations of the reciprocal space coordinates for each detector pixel were performed using the tilt-corrected angles. The position of all visible Bragg reflections on the detector and the corresponding observed sample rotations were used to accurately determine the orientation of the crystal as described in Ref. 42. After mounting and alignment of the Pt sample, the positions of the ≈ 30 Bragg reflections from the bulk crystal were masked using small W pieces, placed directly in front of the 2D detector. This is necessary to prevent damage to the detector by the intense Bragg reflections, while measuring the weak CTR intensities with the unattenuated incident beam. The beamstops manifest as black areas on the detector frames (see Supplementary Figure 8 and missing data points in the CTR profiles). In addition, the incident beam was blocked by a beamstop located about $10\,\text{cm}$ behind the sample, to reduce air scattering background.

Points in reciprocal space were described in terms of the Miller indices ($H\ K\ L$), where H and K correspond to reciprocal lattice unit cell vectors $\vec{b_1}$ and $\vec{b_2}$ in the surface plane and L to a vector $\vec{b_3}$ along the surface normal. For Pt(100) we chose the conventional cubic reciprocal basis with lattice vectors $|\vec{b_1}| = |\vec{b_2}| = |\vec{b_3}| = 2\pi/a$ with $a = 3.9242\,\text{Å}$ being the Pt lattice constant. In the case of Pt(111) we used a hexagonal unit cell with reciprocal lattice vectors of length $|\vec{b_1}| = |\vec{b_2}| = 8\pi/\sqrt{6}a$ and $|\vec{b_3}| = 2\pi/\sqrt{3}a$, which is common in SXRD studies of fcc(111) surfaces.[43] A schematic illustration of the reciprocal space geometry of Pt(111) and Pt(100) is

shown in Supplementary Figure 7. The Bragg reflections of Pt(111) are separated by $\Delta L_{\mathrm{Bragg}} = 3$ and the ones for Pt(001) are separated by $\Delta L_{\mathrm{Bragg}} = 2$ along the CTRs. The absence of some CTRs, such as (1 0 L), (2 1 L), etc. for Pt(100), is related to the chosen fcc unit cell.

Determination of the CTR structure factors. Crystal truncation rod (CTR) data are commonly presented by plotting the structure factor F_{HKL} as a function of L. To determine these structure factors by HESXRD, the reciprocal space is mapped by continuously recording detector frames during a single rotation of the crystal around the surface normal.[30] By summing up all the detector frames recorded during a reciprocal space mapping, the CTRs can be directly visualized (Supplementary Figure 8, vertical lines). Since the unit cell of Pt(100) has a rotational symmetry of 90°, a 110° rotation was sufficient to collect all symmetrically non-equivalent CTRs. An angular resolution of 0.05° was chosen to achieve high enough reciprocal space resolution at the low L values of the (3 1 L) CTR. From these data, the CTR structure factors were determined using the *binoculars* software.[44] Here, first correction factors for solid angle and polarisation are applied to the measured intensities.[45] Then, a 3D representation of the reciprocal space is calculated by binning the intensities of each individual pixel, using the reciprocal space coordinates on each frame. For the analysis of the Pt(100) data, bin sizes of $\Delta H = 0.002$, $\Delta K = 0.002$ and $\Delta L = 0.03$ were used. This corresponds to a series of HK-slices along the CTR, which are separated by the distance ΔL. Within this ΔL range, the structure factor F_{HKL} of the CTR is assumed to be constant and was determined by taking the square root of the integrated X-ray intensity at the CTR position. The background intensity was integrated in a region close to the CTR position and was subtracted from the CTR intensity. A more detailed description of the direct structure factor extraction in recipro-

cal space is given in the paper by Drnec et al.[46]. To obtain the statistical uncertainties σ_2 of each reflection, we extended the *binoculars* software by a package that calculates these uncertainties according to Poisson statistics. The total number of measured reflections in each CTR dataset was between 1922 and 2005. After averaging of symmetry equivalent reflections, between 802 and 808 reflections were available for the structural analysis. The agreement factor ε of the symmetry equivalent reflections was 0.08 ± 0.07. The uncertainties of the averaged reflections were then calculated to $\sigma = \sqrt{\varepsilon^2 F_{HKL}^2 + \sigma_2^2}$.

Fitting of structural models to the CTR data. To obtain the atomic positions of the surface atoms, all CTRs of a given data set were jointly fitted by a surface structural model using a Python-based software, developed by us for the quantitative analysis of HESXRD data. In this software, the structure factors, calculated from the model using kinematic scattering theory,[47] are fitted to the experimentally observed structure factors by the least squares method. A detailed description of the analysis of the CTRs in the double layer region and in the region of oxide formation is given in Supplementary Note 2 and 3, respectively. The statistical errors of the best-fit parameters given in Supplementary Tables 1-4 were calculated with the covariance matrix method.[48] These errors only take into account the goodness of fit and the experimental errors of the observed reflections, which are given by the counting statistics and the agreement factor between symmetry equivalent reflections. Systematic errors due to the chosen fit model are not included here. Those can be estimated from Supplementary Table 4, where for two central parameters, the occupancy and height of the Pt_{ex} atoms, and three characteristic potentials, 1.07 V, 1.12 V and 1.17 V, the results of the best fits obtained by four different surface models are given.

Computational methods. The density functional theory calculations were carried out using the VASP code, version 5.3.5-avx [49]. The PAW method[50] was used to describe the interaction between the core electrons and the valence electron density, described by means of a plane-wave basis set, and the PBE exchange-correlation functional[51]. In the optimization, we used a plane-wave cutoff of $450\,\mathrm{eV}$, the convergence criterion for the atomic forces was $0.05\,\mathrm{eV}\cdot\mathrm{\AA}^{-1}$ and dipole corrections were applied between periodically repeated images in the z-axis. In the 4-layer-thick (3×3) Pt(111) and (3×3) Pt(100) slabs the two topmost layers and the adsorbates were fully relaxed, while the two bottommost layers were fixed. For both slabs the k-point sampling was (4×4×1). H_2 and H_2O were simulated in cubic boxes of $3375\,\mathrm{\AA}^3$, sampling the gamma point only. The free energies were approximated as: $G = E^{DFT} + ZPE - TS + G^{solv}$. The zero-point-energy (ZPE) and vibrational-entropy (TS^{vib}) corrections were calculated within the harmonic oscillator approximation for the adsorbed species, whereas for H_2 and H_2O the values were taken from thermodynamic tables (see Supplementary Tables 5 and 6).[52] Solvation contributions to the adsorption energies (G^{solv}) of H_2O_{ads} and OH_{ads} were taken from previous studies. [53,54] Proton-electron transfers were modelled with the computational hydrogen electrode.[55] The Pourbaix diagrams of Pt(111) and Pt(100) in Extended Data Fig. 5 were built following the methodology described in Ref. 56.

The energetics of Pt dissolution as Pt^{2+} and $PtOH^+$ was evaluated based on the experimental standard dissolution potential of Pt of 1.18 V and that of the reaction, which is 1.20 V.[52] From those two reactions, we conclude that Pt^{2+} is slightly favored over $PtOH^+$, thermodynamically speaking. Besides, we note that the cohesive energy of bulk Pt provided by PBE is 5.54 eV, while in experiments it is 5.87 eV.[57] Thus, a correction of 0.33 eV needs to be applied.

In calculated Pourbaix diagrams (Extended Data Fig. 5), we observe that O_{ads} (i) is more strongly adsorbed on Pt(111) compared to Pt(100) at the same coverage and (ii) adsorbs at twofold bridge sites on Pt(100) and at threefold fcc hollow sites on Pt(111) (Supplementary Table 5). At a given potential, the oxygen coverage (θ_O) is typically larger on Pt(100) with respect to Pt(111), due to lower lateral repulsion, and corresponding well with previous calculations.[56,58]

Acknowledgements

We acknowledge the European Synchrotron Radiation Facility for provision of SXRD facilities, and H. Isern and T. Dufrane for their help with the SXRD experiments. Funding is acknowledged from NSERC (grant RGPIN-2017-04045) and Deutsche Forschungsgemeinschaft (grants MA 1618/23 and CH 1763/5-1).

Author Contributions

All authors performed experimental work and were involved in the experiment design. T.F. and D.J.S.S. analysed SXRD and SFC-ICP-MS data respectively. F.C.-V. performed DFT calculations. T.F., J.D. and O.M.M. prepared the manuscript. All authors were involved in data interpretation and editing of the manuscript.

Competing Interests

The authors declare no competing interests.

Data availability

The raw data has been deposited in the repository (link to the data will be placed here). All other data supporting the findings of this study are available within the article and its Supplementary Information, or from the corresponding author upon reasonable request.

Code availability

The custom software for the analysis of the CTR data and the custom *binoculars* backend for HESXRD structure factor determination are deposited in the repository (link to the data will be placed here). All other software used for this study is publicly available or can be obtained from the corresponding author upon reasonable request.

References

1. Meier, J. C. *et al.* Design criteria for stable Pt/C fuel cell catalysts. *Beilstein J. Nanotech.* **5**, 44–67 (2014).

2. Climent, V. & Feliu, J. M. Thirty years of platinum single crystal electrochemistry. *J. Solid State Electrochem.* **15**, 1297–1315 (2011).

3. Conway, B. E. & Jerkiewicz, G. Surface orientation dependence of oxide film growth at platinum single crystals. *J. Electroanal. Chem.* **339**, 123–146 (1992).

4. You, H., Zurawski, D. J., Nagy, Z. & Yonco, R. M. In-situ x-ray reflectivity study of incipient

oxidation of Pt(111) surface in electrolyte solutions. *J. Chem. Phys.* **100**, 4699–4702 (1994).

5. Tidswell, I., Markovic, N. & Ross, P. Potential dependent surface structure of the Pt(1 1 1) electrolyte interface. *J. Electroanal. Chem.* **376**, 119 – 126 (1994).

6. Wakisaka, M., Udagawa, Y., Suzuki, H., Uchida, H. & Watanabe, M. Structural effects on the surface oxidation processes at pt single-crystal electrodes studied by x-ray photoelectron spectroscopy. *Energy Environ. Sci.* **4**, 1662 (2011).

7. Gómez-Marín, A. M. & Feliu, J. M. Oxide growth dynamics at Pt(111) in absence of specific adsorption: A mechanistic study. *Electrochim. Acta* **104**, 367–377 (2013).

8. Tanaka, H. *et al.* Infrared reflection absorption spectroscopy of OH adsorption on the low index planes of pt. *Electrocatalysis* **6**, 295–299 (2014).

9. Sugimura, F., Nakamura, M. & Hoshi, N. The oxygen reduction reaction on kinked stepped surfaces of pt. *Electrocatalysis* **8**, 46–50 (2016).

10. Huang, Y.-F., Kooyman, P. J. & Koper, M. T. M. Intermediate stages of electrochemical oxidation of single-crystalline platinum revealed by in situ Raman spectroscopy. *Nat. Commun.* **7**, 12440 (2016).

11. Sugimura, F. *et al.* In situ observation of Pt oxides on the low index planes of Pt using surface enhanced Raman spectroscopy. *Phys. Chem. Chem. Phys.* **19**, 27570–27579 (2017).

12. Furuya, N. & Shibata, M. Structural changes at various Pt single crystal surfaces with potential cycles in acidic and alkaline solutions. *J. Electroanal. Chem.* **467**, 85–91 (1999).

13. Itaya, K., Sugawara, S., Sashikata, K. & Furuya, N. Insitu scanning tunneling microscopy of platinum (111) surface with the observation of monatomic steps . *J. Vac. Sci. Technol. A* **8**, 515–519 (1990).

14. Lopes, P. P. *et al.* Relationships between Atomic Level Surface Structure and Stability/Activity of Platinum Surface Atoms in Aqueous Environments. *ACS Catal.* **6**, 2536–2544 (2016).

15. Lopes, P. P. *et al.* Dynamics of electrochemical Pt dissolution at atomic and molecular levels. *J. Electroanal. Chem.* **819**, 123–129 (2018).

16. Sandbeck, D. J. *et al.* Dissolution of Platinum Single Crystals in Acidic Medium. *ChemPhysChem* **20**, 2997–3003 (2019).

17. Ruge, M. *et al.* Structural Reorganization of Pt(111) Electrodes by Electrochemical Oxidation and Reduction. *J. Am. Chem. Soc.* **139**, 4532–4539 (2017).

18. Ruge, M. *et al.* Electrochemical oxidation of smooth and nanoscale rough Pt(111): An in situ surface X-ray scattering study. *J. Electrochem. Soc* **164**, H608–H614 (2017).

19. Jacobse, L., Huang, Y.-F., Koper, M. T. M. & Rost, M. J. Correlation of surface site formation to nanoisland growth in the electrochemical roughening of Pt(111). *Nat. Mater.* **17**, 277–282 (2018).

20. Arulmozhi, N., Esau, D., Lamsal, R. P., Beauchemin, D. & Jerkiewicz, G. Structural transformation of monocrystalline platinum electrodes upon electro-oxidation and electro-dissolution. *ACS Catal.* **8**, 6426–6439 (2018).

21. Topalov, A. A. *et al.* Dissolution of Platinum: Limits for the Deployment of Electrochemical Energy Conversion? *Angew. Chem., Int. Ed.* **51**, 12613–12615 (2012).

22. Gómez-Marín, A. M. & Feliu, J. M. Pt(111) surface disorder kinetics in perchloric acid solutions and the influence of specific anion adsorption. *Electrochim. Acta* **82**, 558–569 (2012).

23. Drnec, J. *et al.* Initial stages of Pt(111) electrooxidation: dynamic and structural studies by surface X-ray diffraction. *Electrochim. Acta* **224**, 220 – 227 (2017).

24. Drnec, J., Harrington, D. & Magnussen, O. Electrooxidation of Pt(111) in acid solution. *Curr. Op. Electrochem.* **4**, 69–75 (2017).

25. Liu, Y., Barbour, A., Komanicky, V. & You, H. X-ray Crystal Truncation Rod Studies of Surface Oxidation and Reduction on Pt(111). *J. Phys. Chem. C* **120**, 16174–16178 (2016).

26. Fantauzzi, D., Mueller, J. E., Sabo, L., van Duin, A. C. T. & Jacob, T. Surface Buckling and Subsurface Oxygen: Atomistic Insights into the Surface Oxidation of Pt(111). *ChemPhysChem* **16**, 2797–2802 (2015).

27. Eslamibidgoli, M. J. & Eikerling, M. H. Atomistic Mechanism of Pt Extraction at Oxidized Surfaces: Insights from DFT. *Electrocatalysis* **7**, 345–354 (2016).

28. Gu, Z. & Balbuena, P. B. Chemical Environment Effects on the Atomic Oxygen Absorption into Pt(111) Subsurfaces. *J. Phys. Chem. C* **111**, 17388–17396 (2007).

462 29. Rodes, A., Zamakhchari, M. A., El Achi, K. & Clavilier, J. Electrochemical behaviour of
463 Pt(100) in various acidic media: Part I. On a new voltammetric profile of Pt(100) in perchloric
464 acid and effects of surface defects. *J. Electroanal. Chem.,* **305**, 115–129 (1991).

465 30. Gustafson, J. *et al.* High-Energy Surface X-ray Diffraction for Fast Surface Structure Deter-
466 mination. *Science* **343**, 758–761 (2014).

467 31. Devarajan, S. P., Hinojosa, J. A. & Weaver, J. F. STM study of high-coverage structures of
468 atomic oxygen on Pt(1 1 1): p(2 $\times$ 1) and Pt oxide chain structures. *Surf. Sci.* **602**, 3116–3124
469 (2008).

470 32. Van Spronsen, M. A., Frenken, J. W. & Groot, I. M. Observing the oxidation of platinum. *Nat.*
471 *Commun.* **8** (2017).

472 33. Xing, L., Jerkiewicz, G. & Beauchemin, D. Ion exchange chromatography coupled to induc-
473 tively coupled plasma mass spectrometry for the study of pt electro-dissolution. *Anal. Chim.*
474 *Acta* **785**, 16 – 21 (2013).

475 34. Cherevko, S., Kulyk, N. & Mayrhofer, K. J. Durability of platinum-based fuel cell electrocat-
476 alysts: Dissolution of bulk and nanoscale platinum. *Nano Energy* **29**, 275 – 298 (2016).

477 35. Cherevko, S., Topalov, A. A., Zeradjanin, A. R., Keeley, G. P. & Mayrhofer, K. J. J.
478 Temperature-Dependent Dissolution of Polycrystalline Platinum in Sulfuric Acid Electrolyte.
479 *Electrocatalysis* **5**, 235–240 (2014).

480 36. Geiger, S. *Stability investigations of iridium-based catalysts towards acidic water splitting*.
481 doctoralthesis, Ruhr-Universität Bochum, Universitätsbibliothek (2018).

37. Lamsal, R. P., Jerkiewicz, G. & Beauchemin, D. Enhancement of the capabilities of inductively coupled plasma mass spectrometry using monosegmented flow analysis. *Anal. Chem.* **90**, 13842–13847 (2018).

38. Sandbeck, D. J. S. *On the Dissolution of Platinum: From Fundamental to Advanced Catalytic Materials*. doctoralthesis, Friedrich-Alexander-Universität Erlangen-Nürnberg (FAU) (2020).

39. Magnussen, O. M., Krug, K., Ayyad, A. H. & Stettner, J. In situ diffraction studies of electrode surface structure during gold electrodeposition. *Electrochim. Acta* **53**, 3449–3458 (2008).

40. Drnec, J. *et al.* Pt oxide and oxygen reduction at Pt(111) studied by surface X-ray diffraction. *Electrochem. Commun.* **84**, 50–52 (2017).

41. Ashiotis, G. *et al.* The fast azimuthal integration Python library: PyFAI. *J. Appl. Crystallogr.* **48**, 510–519 (2015).

42. Busing, W. R. & Levy, H. A. Angle calculations for 3- and 4-circle X-ray and neutron diffractometers. *Acta Crystallogr.* **22**, 457–464 (1967).

43. Wang, J., Ocko, B., Davenport, A. & Isaacs, H. In situ X-ray-diffraction and -reflectivity studies of the Au(111)/ electrolyte interface: reconstruction and anion adsorption. *Phys. Rev. B* **46**, 10321–10338 (1992).

44. Roobol, S., Onderwaater, W., Drnec, J., Felici, R. & Frenken, J. BINoculars: Data reduction and analysis software for two-dimensional detectors in surface X-ray diffraction. *J. Appl. Crystallogr.* **48**, 1324–1329 (2015).

501 45. Vlieg, E. Integrated Intensities Using a Six-Circle Surface X-ray Diffractometer. *J. Appl.*
502 *Crystallogr.* **30**, 532–543 (1997).

503 46. Drnec, J. *et al.* Integration techniques for surface X-ray diffraction data obtained with a two-
504 dimensional detector. *J. Appl. Crystallogr.* **47**, 365–377 (2014).

505 47. Feidenhans'l, R. Surface structure determination by X-ray diffraction. *Surf. Sci. Rep.* **10**,
506 105–188 (1989).

507 48. Press, W. H., Teukolsky, S. A., Vettering, W. T. & Flannery, B. P. *Numerical Recipes in C:*
508 *The Art of Scientific Computing. Second Edition* (Cambridge University Press, 1992).

509 49. Kresse, G. & Furthmüller, J. Efficient iterative schemes for ab initio total-energy calculations
510 using a plane-wave basis set. *Phys. Rev. B* **54**, 11169–11186 (1996).

511 50. Kresse, G. & Joubert, D. From ultrasoft pseudopotentials to the projector augmented-wave
512 method. *Phys. Rev. B* **59**, 1758–1775 (1999).

513 51. Perdew, J. P., Burke, K. & Ernzerhof, M. Generalized Gradient Approximation Made Simple.
514 *Phys. Rev. Lett.* **77**, 3865–3868 (1996).

515 52. Lide, D. R. (ed.) *CRC Handbook of Chemistry and Physics, 85th Edition* (CRC Press, 2005).

516 53. Calle-Vallejo, F., de Morais, R., Illas, F., Loffreda, D. & Sautet, P. Affordable Estimation of
517 Solvation Contributions to the Adsorption Energies of Oxygenates on Metal Nanoparticles. *J.*
518 *Phys. Chem. C* **123**, 5578–5582 (2019).

519 54. He, Z.-D., Hanselman, S., Chen, Y.-X., Koper, M. T. M. & Calle-Vallejo, F. Importance of
520 Solvation for the Accurate Prediction of Oxygen Reduction Activities of Pt-Based Electrocat-
521 alysts. *J. Phys. Chem. Lett.* **8**, 2243–2246 (2017).

522 55. Nørskov, J. K. *et al.* Origin of the Overpotential for Oxygen Reduction at a Fuel-Cell Cathode.
523 *J. Phys. Chem. B* **108**, 17886–17892 (2004).

524 56. Hansen, H. A., Rossmeisl, J. & Nørskov, J. K. Surface Pourbaix diagrams and oxygen reduc-
525 tion activity of Pt, Ag and Ni(111) surfaces studied by DFT. *Phys. Chem. Chem. Phys.* **10**,
526 3722–3730 (2008).

527 57. Janthon, P. *et al.* Bulk Properties of Transition Metals: A Challenge for the Design of Universal
528 Density Functionals. *J. Chem. Theory Comput.* **10**, 3832–3839 (2014).

529 58. Bizzotto, F. *et al.* Examining the Structure Sensitivity of the Oxygen Evolution Reaction on Pt
530 Single-Crystal Electrodes: A Combined Experimental and Theoretical Study. *ChemPhysChem*
531 **20** (2019).

Extended Data Figures

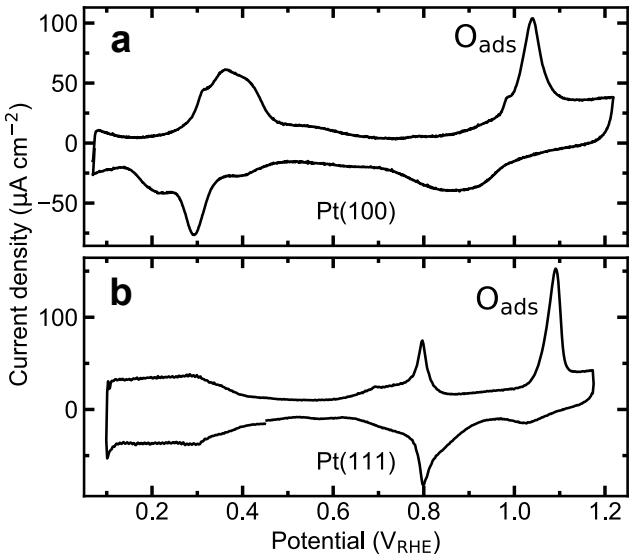

Extended Data Fig. 1. Cyclic voltammograms measured in the electrochemical cell used for the Surface X-ray Diffraction measurements. Cyclic voltammograms of **(a)** Pt(100) and **(b)** Pt(111) in 0.1 M $HClO_4$ with a scan rate of $50\,\mathrm{mV/s}$.

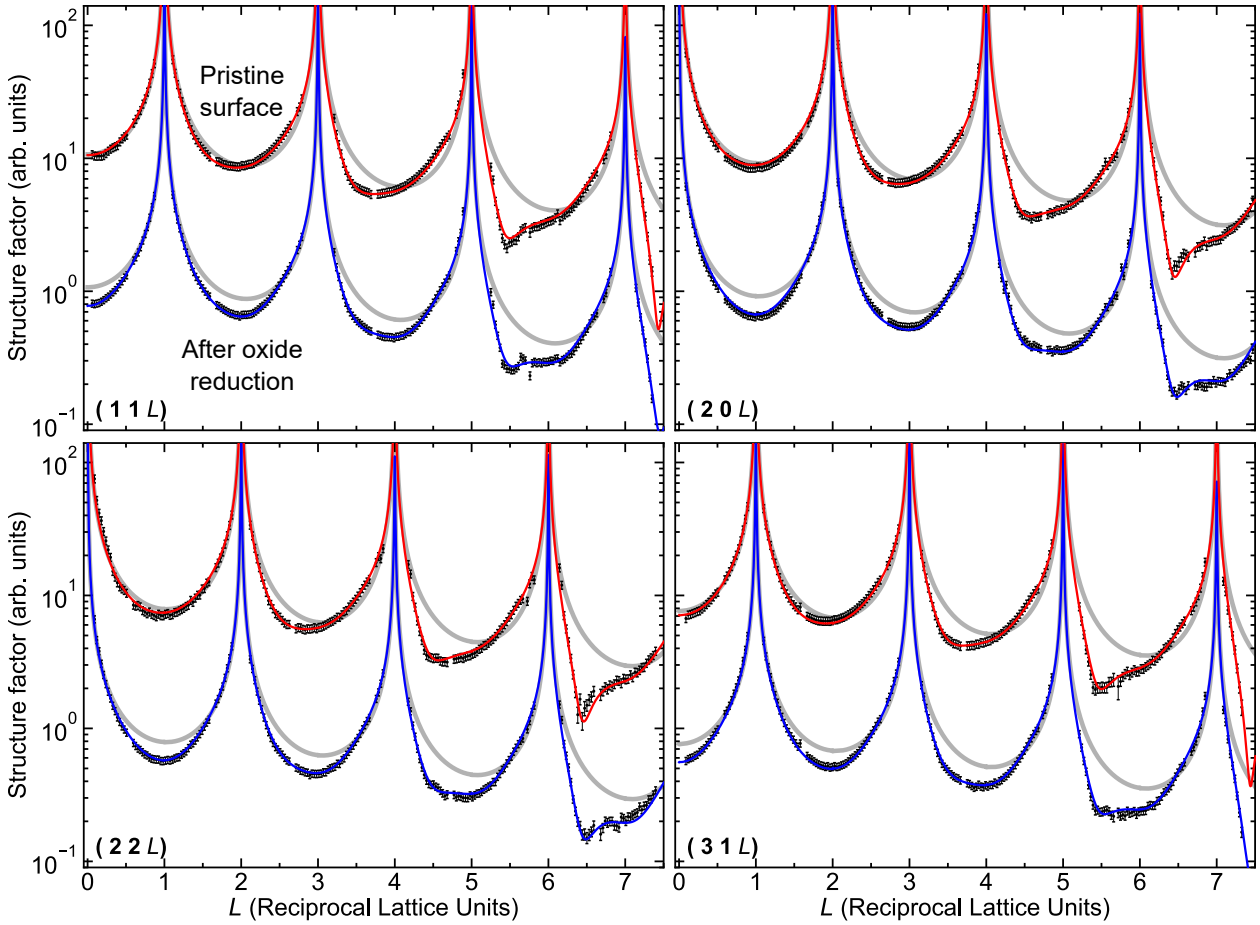

Extended Data Fig. 2. Surface structure of Pt(100) at 0.12 V prior surface oxidation and after oxide reduction. (a): Crystal truncation rods (CTR) of the pristine Pt(100) surface and the the roughened surface after oxidation at 1.17 V and subsequent reduction at 0.12 V. The grey lines indicate the CTRs of a bulk terminated Pt(100) surface. The decreased of the CTR after surface oxidation can be attributed to the formation of adatoms Pt_{ad} and vacancies in the Pt_1 layer. Best fits with a quantitative model (solid blue line) that includes these surface defects result in a Pt_{ad} coverage of 0.07 ML.

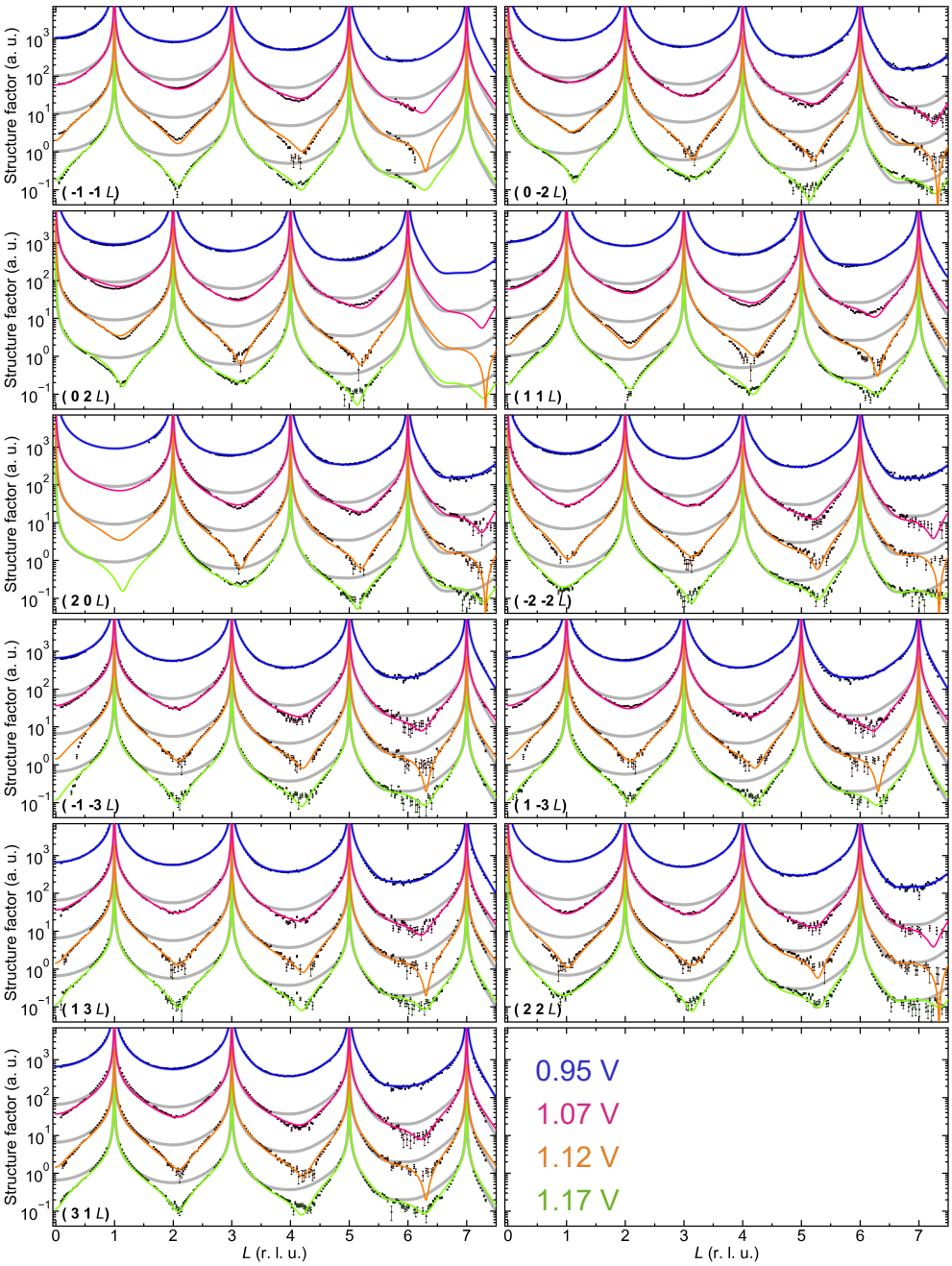

Extended Data Fig. 3. Crystal truncation rods and corresponding CTR fits of Pt(100) close to and in the region of oxide formation. Crystal truncation rods (CTR) of Pt(100) at a potential slightly negative (0.95 V) and three potentials positive (1.07, 1.12 and 1.17 V) of the O_{ads} peak in the cyclic voltammogram (Fig. 1b, Extended Data Fig. 1). Solid lines are the corresponding CTR fits. The CTRs for the different potentials are offset to each other by a factor 10 and shown together with the CTR fits of the smooth surface at 0.95 V (grey lines). Details on the CTR fits are given in the Supplementary Note 3 and the corresponding structural parameters are given in Supplementary Table 4.

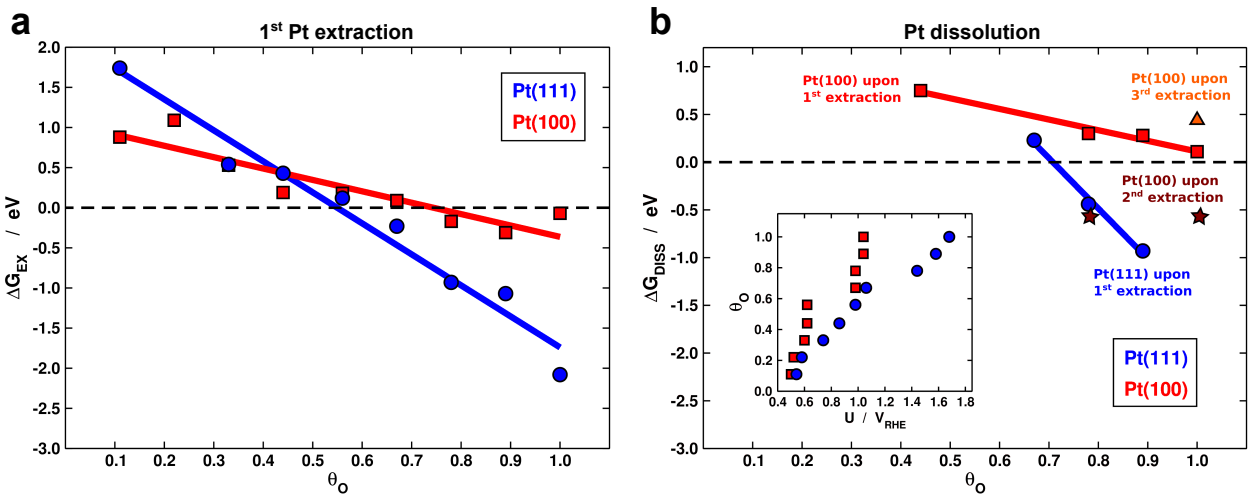

Extended Data Fig. 4. Gibbs energy for the first Pt extraction and the subsequent dissolution of Pt. **(a)** Oxygen coverage θ_O dependent Gibbs energy change ΔG for the extraction of the first atom on Pt(111) and Pt(100). **(b)** ΔG for the dissolution of the extracted atom after 1 $_{st}$ extraction on Pt(111) and 1 st, 2 nd and 3 rd extraction on Pt(100). The correspondence between the oxygen coverage θ_O and potential U is in the inset of **(b)**.

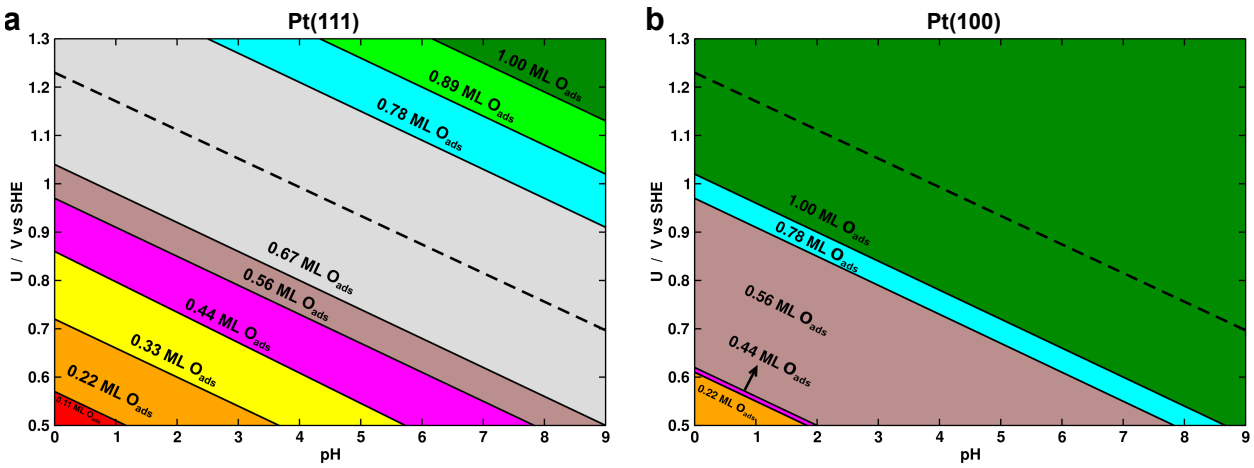

Extended Data Fig. 5. Pourbaix diagrams for O adsorption. Pourbaix diagram of **(a)** Pt(111) and **(b)** Pt(100). The dashed line represents the oxygen reduction reaction ($O_2 + 4\,(H^+ + e^-) \longrightarrow 2\,H_2O$).

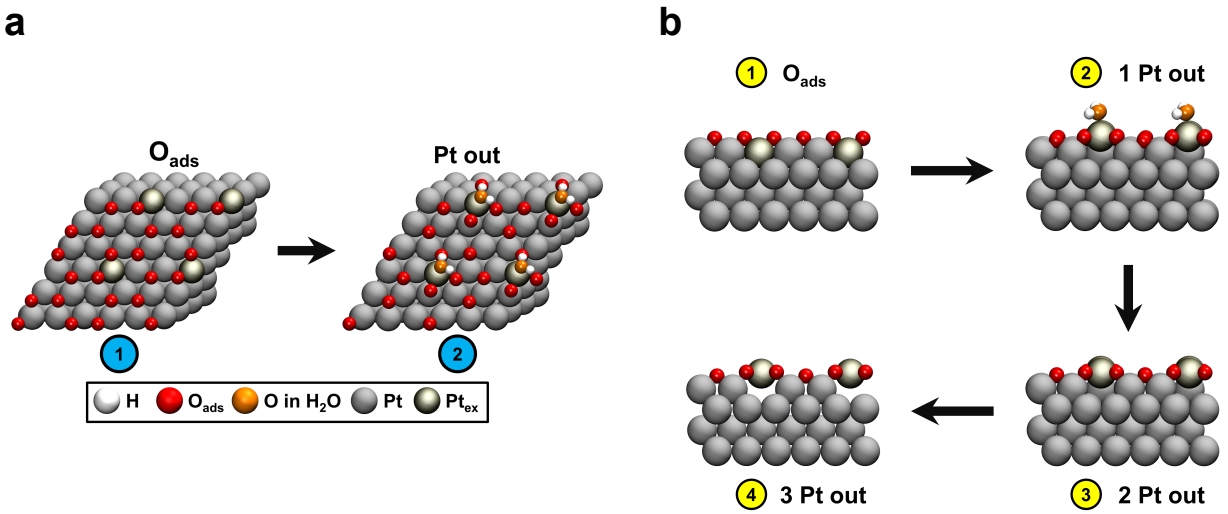

Extended Data Fig. 6. Additional views of the lowest-energy structures in the process of Pt extraction. **(a)** Top view of the Pt extraction process on Pt(111). **(b)** Side view of the Pt extraction process on Pt(100).